Relationship Between GOES-R Series Spacecraft Operational Anomalies and In Situ 30 eV–3-MeV Electron Measurements

Brian T. Kress, Juan V. Rodriguez, Natalia Y. Buzulukova, Robert J. Redmon, Janet L. Machol, John L. Fiorello, Michael A. Roza, and Robert M. Meloy

***Abstract*— The first two of NOAA's Geostationary Operational Environmental Satellite (GOES)-R series spacecraft, GOES-16, and GOES-17, were launched in November 2016 and March 2018, respectively. Space weather instruments on board GOES-R Series spacecraft include the low- and high-energy magnetospheric particle sensors, MPS-LO and MPS-HI. These sensors measure 30-eV to ∼3-MeV electrons in 25 differential energy channels and one integral (>2 MeV) channel. Since launch, a growing catalog of recurring GOES-R series operational anomalies has been maintained by the GOES-R program. A subset of the anomalies show a clear relation to ambient electron fluxes. These anomalies are primarily associated with the solar pointing platform (SPP) instruments and their interface with the spacecraft. The list of GOES-R operational anomalies and continuous in situ electron measurements from the same satellites provide an unsurpassed opportunity to study the interrelation between spacecraft errors and the ambient electron environment. In this work, we focus on one type of spacecraft anomaly involving telemetry between the extreme ultraviolet and X-ray irradiance sensors (EXIS) and the spacecraft. It is found that these anomalies occur more frequently when ambient electron flux levels are elevated. Comparisons with full distributions of measured fluxes and distributions of fluxes preceding anomalies show that the anomaly occurrences are most well associated with the elevation of ∼130-keV electrons above normal levels, implicating shallow internal charging by electrons in the low hundreds of kiloelectron volts. This is confirmed by results from superposed epoch analysis (SEA) showing strong peaks in MPS-HI energy channels in the low hundreds of kiloelectron volts preceding the anomalies by ∼30 min. Analysis of the local time dependence of the anomalies and measured fluxes reveal that there is a delay between the peak in ambient electron flux and anomaly occurrences suggesting a charging timescale of ∼30 min to several hours.**

***Index Terms*— Electrostatic discharges (ESDs), low Earth orbit satellites, plasma measurements, radiation effects, space radiation.**

I. Introduction

ENERGETIC electrons in space cause charging in spacecraft components which can lead to electrostatic discharges (ESDs) that damage electronics and interfere with electronic operations. Spacecraft charging is usually subdivided into two categories: surface charging and internal charging. Surface charging is associated with enhancements in ambient electron fluxes in the energy range ∼5–10 s of keV, which can produce elevated potentials on spacecraft surfaces on a timescale of seconds to minutes [1, pp. 27 and 36], [2], [3]. Internal charging occurs when hundreds of kiloelectron volt to megaelectron volt electrons penetrate into dielectric materials causing charge buildup [1], [4], [5, p. 27]. The timescale for the buildup of charge responsible for internal charging is thought to be much longer than surface charging, ranging from hours to days [3], [6], [7]. Internal dielectric charging can cause ESDs that degrade dielectric materials in microelectronic devices and corrupt digital logic and telemetry, e.g., produce electromagnetic pulses causing spurious commands [8]. Although ESDs due to internal charging have been found to cause the majority of environmentally related anomalies on spacecraft, ESDs due to surface charging have caused the most serious anomalies, i.e., those that have resulted in the loss of mission [9].

Anomalies due to internal charging are often attributed to megaelectron volt electron fluxes, and internal charging timescales are considered to be ∼days [10], [11], [12], [13], [14], [15]. Baker et al. [16] attributed anomalies on-board geostationary spacecraft Intelsat-K and Anik-E to deep dielectric charging by >1-MeV electrons and in general cite 0.5- to 10.0-MeV electrons as the source of deep dielectric charging. Wrenn and Smith [6] associate phantom commands on geostationary satellites with Geostationary Operational Environmental Satellite (GOES)-7 >2-MeV daily electron

Manuscript received 18 October 2023; revised 1 March 2024; accepted 28 March 2024. Date of publication 16 May 2024; date of current version 14 August 2024. This work was supported in part by National Aeronautics and Space Administration (NASA) Living With a Star Program (LWS) under Grant 80NSSC19K0085 and Grant NNG19OB09A and in part by the Geostationary Operational Environmental Satellite (GOES)-R series Program and the National Centers for Environmental Information (NCEI) through the National Oceanic and Atmospheric Administration (NOAA) Cooperative Agreements under Grant NA15OAR4320137 and Grant NA17OAR4320101. The review of this article was arranged by Senior Editor S. T. Lai. *(Corresponding author: Brian T. Kress.)*

Brian T. Kress, Juan V. Rodriguez, and Janet L. Machol are with the Cooperative Institute for Research in the Environmental Sciences, University of Colorado Boulder, Boulder, CO 80309 USA, and also with the NOAA National Centers for Environmental Information, Boulder, CO 80305 USA (e-mail: brian.kress@noaa.gov; juan.rodriguez@noaa.gov; janet.machol@noaa.gov).

Natalia Y. Buzulukova is with the Geospace Physics Laboratory, NASA Goddard Space Flight Center, Greenbelt, MD 20771 USA, and also with the Department of Astronomy, University of Maryland, College Park, MD 20742 USA (e-mail: nbuzulukova@gmail.com).

Robert J. Redmon is with the NOAA National Centers for Environmental Information, Boulder, CO 80305 USA (e-mail: rob.redmon@noaa.gov).

John L. Fiorello and Michael A. Roza are with the NASA Goddard Space Flight Center, Greenbelt, MD 20771 USA (e-mail: john.l.fiorello@nasa.gov; michael.a.roza@nasa.gov).

Robert M. Meloy is with Science Systems and Applications Inc., Lanham, MD 20706 USA (e-mail: robert.m.meloy@nasa.gov).

Color versions of one or more figures in this article are available at https://doi.org/10.1109/TPS.2024.3390658.

Digital Object Identifier 10.1109/TPS.2024.3390658

fluence and estimate charging times of two days, but also note clustering in local time of the anomalies. Because the intensity of >2-MeV electron flux has been linked to spacecraft operational errors in geostationary orbit, it is used by the NOAA Space Weather Prediction Center (SWPC) as a warning to spacecraft operators of increased likelihood of effects due to internal charging. SWPC issues its real-time radiation belt alerts when the >2-MeV flux exceeds 1000 (electrons/cm^2·sr·s).

ESDs due to internal charging have also been associated with ambient electron fluxes in the hundreds of kiloelectron volts. Fennell et al. [5], [17] used measurements from the Spacecraft Charging AT High Altitudes (SCATHA) satellite to show there is a dramatic increase in the rate of internal discharges when the >300-keV electron flux exceeds 10^5 electrons/(cm^2·s·sr), and attributed SCATHA ESD rates peaked near noon local time to internal charging by hundreds of kiloelectron volt electrons. Fennell et al. [17] also showed that a moderate hardening of the spectrum in the 10–100-keV range produced significantly larger ESDs and higher ESD rates. Ferguson et al. [18] present evidence that the Galaxy 15 spacecraft anomaly on April 5, 2010 was caused by surface charging or deep-dielectric charging and note that internal charging typically requires high fluences of charged particles with energies of 200 keV or more.

Analysis of the local time dependence of spacecraft anomalies is a standard approach that has been used to infer electron energy range and type of charging that is the source of the anomalies [2], [6], [8], [14], [19], [20]; Farthing et al. [19] associated anomalies clustered in the morning sector with individual injections identified in ground magnetometer data and determined that the time interval between the injections and anomalies was consistent with the drift period of 10–15-keV electrons. Spacecraft anomaly occurrences clustered in the morning sector are usually attributed to surface charging by hundreds of kiloelectron volt electrons [3], [14]. In general, tens of kiloelectron volt fluxes decrease and radiation belt energies (hundreds of kiloelectron volts to megaelectron volts) increase from midnight to noon local time along geosynchronous orbit, due to dayside compression of the geomagnetic field. Spacecraft anomaly occurrences clustered near noon local time are considered an indicator of internal charging [14], [17], [21].

Strong correlations between fluxes over a broad range of radiation belt electron energies make determining the electron energy range causing a given spacecraft anomaly more difficult. The goal of this work is to link one particular type of GOES-R series spacecraft anomaly with electron flux enhancements in a specific energy range, as measured by particle detectors flown on-board the same spacecraft where the anomaly occurs. Each GOES-R series spacecraft carries the Space Environment In Situ Suite (SEISS) [22], [23], which includes low- and high-energy magnetospheric particle sensors, MPS-LO and MPS-HI. Collectively, MPS-LO and MPS-HI measure electrons with energies from 30 eV to 2.9 MeV in 25 differential energy channels, and >2-MeV electrons in an integral channel.

The results presented in this article use data from GOES-16 and -17, which were launched in November 2016 and March 2018, respectively. Since launch, a number of recurring GOES-R series spacecraft system errors have been logged by the GOES-R program. This study is focused on a Space Wire telemetry error between the extreme ultraviolet and X-ray irradiance sensors (EXIS) [24], [25] and the spacecraft. A description of the EXIS telemetry error is provided in Section II. This is followed by brief overviews of MPS-LO and MPS-HI in Section III. For more comprehensive descriptions of MPS-LO and MPS-HI design, operation, and ground calibrations see [22], [26]. Full distributions of fluxes in each of the MPS-LO and MPS-HI energy channels are compared with distributions of flux levels preceding the EXIS telemetry errors. Analysis and results are presented in Section IV, and finally, summary and discussion in Section V.

II. EXIS Space Wire Transmission Anomaly

A number of GOES-R series spacecraft operational error types occur frequently. An automated system has been implemented to search telemetry and alarm data files for specific types of memory errors and log dates and times of each event. In this study, we examine the relation between EXIS Space Wire transaction (EXS_SPW) errors and in situ energetic electron measurements. EXIS is mounted on the SPP, which provides a stable platform that tracks the seasonal and daily movement of the sun relative to the spacecraft. All command and telemetry between EXIS and the spacecraft is handled via the space wire interface. A possible source of the EXS_SPW anomalies is charging/discharging of the space wire cable handling telemetry between the SPP and the spacecraft. Anomalies caused by exposed cables have been investigated previously [8], [27]. The EXS_SPW anomaly does not significantly degrade EXIS operations or science data. The EXS_SPW errors are chosen for two reasons: 1) a total of approximately 1750 GOES-16 and -17 EXS_SPW events have been logged through December 2021, providing good statistics and 2) the EXS_SPW errors exhibit a clear association with periods of elevated energetic electron fluxes.

III. GOES-R Series Magnetospheric Particle Sensors

The GOES-R series space weather instruments include MPS-LO and MPS-HI. Real time data from MPS-LO and MPS-HI are used by SWPC for monitoring spacecraft surface and internal charging hazard levels. MPS-LO measures ions and electrons in the magnetosphere at thermal energies (∼1 keV at geosynchronous). Measurement of 30 eV–30 keV electrons by MPS-LO is a new capability not previously flown on GOES satellites. MPS-HI measures electrons at radiation belt energies. The primary operational use for MPS-HI is to monitor the Earth's outer radiation belts. Radiation belt electrons are a source of charging of internal spacecraft components. The MPS-HI E11 >2-MeV electron channel is currently used for NOAA's NWS SWPC radiation belt alerts.

The GOES spacecraft operate in geostationary orbits in the geographic equatorial plane (0°N latitude, 35 786 km).

GOES-16 MPS began collecting data in January 2017 at the GOES checkout location at 89.5° W longitude, then was moved during November 30–December 11, 2017 to its current location at the GOES-East position at 75.2° W longitude. At 75°–90° W longitudes, the geomagnetic equator is ≈10° south of the geographic equator. GOES-17 MPS began collecting data in May 2018 at 89.5°W longitude, then was moved during October 24–November 13, 2018 to the GOES-West position at 137.2°W longitude, where it remained through the period of data collection used for this study, up to the end of 2021. At 137.2°W, the geomagnetic equator is ≈5° south of the geographic equator.

A. Low-Energy Magnetospheric Particle Sensor

MPS-LO consists of two electrostatic analyzers (ESAs) based on the Special Sensor J (SSJ/5) flown on the Defense Meteorological Satellite Program satellites [28], [29]. MPS-LO measures electrons and ions in 15 energy channels between 0.03 and 30 keV in 14 angular zones (viewing directions) in a fan-in the north–south plane, each with a 15° field-of-view. The south viewing ("right") sensor head (RSH) has seven zones labeled Z1–Z5, Z6R, and Z7R in south to north order. The north viewing ("left") sensor head (LSH) has seven additional zones labeled Z6L, Z7L, and Z8–Z12 in south-to-north order. There are two pairs of overlapping zones: Z6R and Z6L centered at 7.5° south of the geographic equatorial plane and Z7R and Z7L centered at 7.5° north of the geographic equatorial plane; thus, there are 12 unique look directions spanning 180° in the north–south meridional plane. (See the vertical axes in the left panels of Figs. 3 and 4, respectively, for a full listing of MPS-LO zone labels and corresponding look directions with respect to the geographic equator.) During each 1-s ESA sweep, counts are accumulated at each energy for 0.0615 s, and the complete energy-angle distribution of fluxes is reported for electrons and ions every second. MPS-LO channel energies are listed in Table I.

B. High-Energy Magnetospheric Particle Sensor

MPS-HI is comprised of five solid-state electron telescopes and five solid-state proton telescopes, with 30° full cone angle fields-of-view, arranged in a fan-in a meridional plane and centered at 0°, ±35°, and ±70° above/below to the geographic equatorial plane. The five MPS-HI electron telescopes are denoted by ETel-5, ETel-2, ETel-4, ETel-1, and ETel-3, in order of southmost to northmost viewing direction when the spacecraft is upright. MPS-HI reports electron fluxes in ten differential channels with effective energies from 70 keV to 2.9 MeV plus a >2-MeV integral channel and proton fluxes in 11 differential channels spanning 80–12 000 keV. MPS-HI also includes two dosimeters under hemispherical shields of 100 mils (0.254 cm) and 250 mils (0.635 cm) aluminum. Fluxes are reported on a one second cadence in Level-1b data, and 1- and 1-min averages are provided in Level-2 (L2) data. The MPS-HI L2 5-min averaged electron fluxes are used for this study. MPS-HI nominal electron channel center energies are given in Table I. Unit and telescope specific effective energies obtained from bowtie analysis of the electron channel response functions are available from [26].

TABLE I
GOES-R SERIES MPS-LO AND MPS-HI ELECTRON ENERGY CHANNELS

MPS-LO	MPS-HI
E15: 30 eV	E1: 72 keV
E14: 49 eV	E2: 131 keV
E13: 81 eV	E3: 181 keV
E12: 130 eV	E4: 275 keV
E11: 220 eV	E5: 379 keV
E10: 350 eV	E6: 546 keV
E9: 580 eV	E7: 863 keV
E8: 950 eV	E8: 1.49 MeV
E7: 1,550 eV	E9: 1.97 MeV
E6: 2,550 eV	E10: 2.90 MeV
E5: 4,820 eV	E11: >2 MeV
E4: 6,280 eV	
E3: 11,200 eV	
E2: 18,300 eV	
E1: 30,000 eV	

IV. ANALYSIS

The GOES-16 and -17 Magnetospheric Particle Sensors began collecting data in January 2017 and May 2018, respectively. The EXS_SPW anomalies included in this analysis are from the period January 2017 to the end of 2021. In total, the analysis includes 846 GOES-16 and 787 GOES-17 EXS_SPW anomalies logged during 2017–2021; however, not all of these anomalies are included in the analysis of each MPS-LO and MPS-HI energy channel due to incomplete data coverage and bad or missing records.

In general, the EXS_SPW anomalies are found to occur in conjunction with periods of heightened radiation belt fluxes. Clusters of EXS_SPW anomalies are also associated with high solar wind speeds, which are a driver of prompt substorm acceleration of electrons up to hundreds of kiloelectron volts, see [30]. GOES-16 MPS-LO and MPS-HI electron channel fluxes from a period with a high EXS_SPW anomaly occurrence rate (October 22–31, 2019) are shown in Fig. 1. The MPS differential flux traces appear with energies in order from lowest (MPS-LO E15, 30 eV) in the top panel to the highest (MPS-HI E10, 2.9 MeV) near the bottom of the middle panel. The MPS-HI E11 >2-MeV channel flux is shown by the black trace in the bottom panel. The times of EXS_SPW anomalies are shown by vertical black dashed lines. This anomaly cluster is clearly associated with a period of enhanced radiation belt fluxes.

In the example shown in Fig. 1, there are separate cases where the anomalies appear to be associated with enhancement peaks in electron volt, kiloelectron volt, and/or megaelectron volt energies. Note, however, that the first anomaly in the cluster appears >12 h after the highest enhancement in MPS-LO electron fluxes that occurs during the period spanning the anomaly cluster, in energy channels up to 51 keV. Also note that the first anomaly in the cluster occurs prior to the enhancement in the MPS-HI E11 >2-MeV electron channel. A tentative conclusion drawn from this single example is that the EXS_SPW anomalies are due to electrons in the low hundreds of kiloelectron volts, which are significantly enhanced throughout the period of the anomaly cluster. This conclusion is borne out by statistical results presented below.

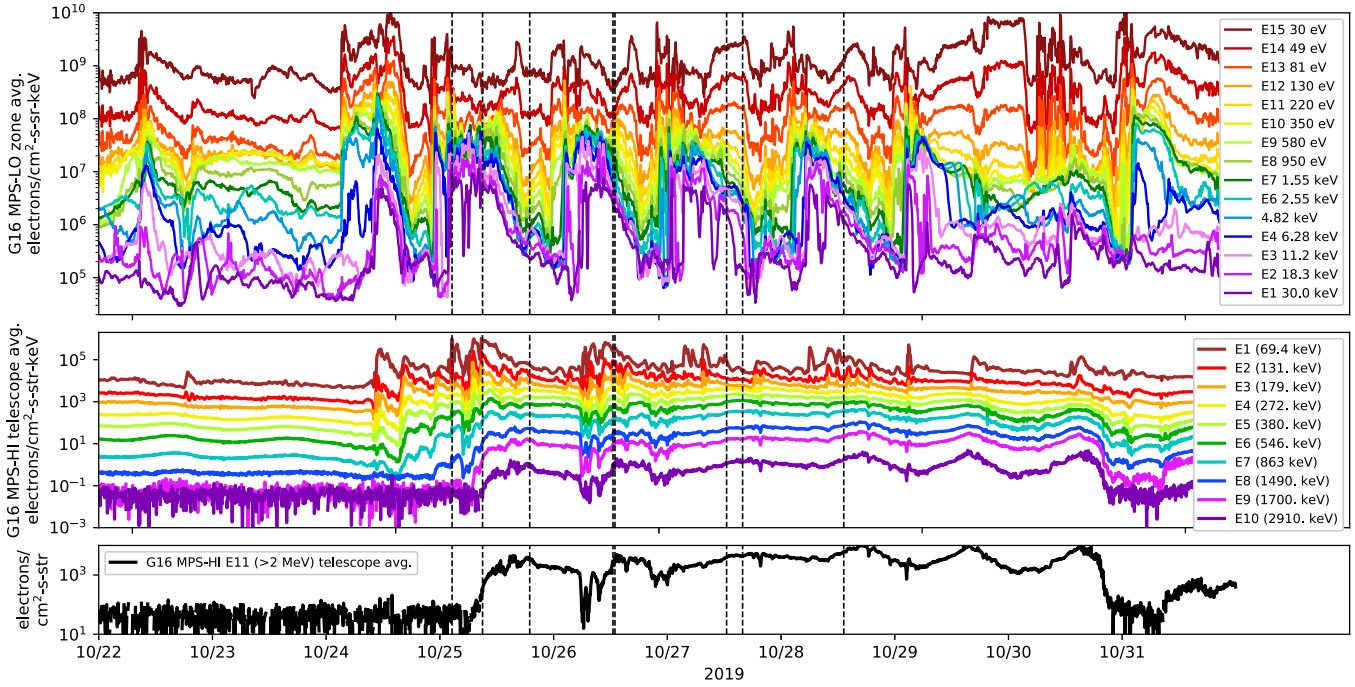

Fig. 1. GOES-16 MPS-LO and MPS-HI electron data time series from a period of enhanced radiation belt fluxes during October 22–31, 2019. Zone- and Telescope-averaged fluxes from all MPS-LO and MPS-HI channels (30 eV–>2 MeV) are shown. The vertical dashed lines show the times of the EXS_SPW anomalies. In general, periods of enhanced electron fluxes like this one are accompanied by clusters of GOES-R series EXIS telemetry anomalies.

A. Comparison With Full and Anomaly Flux Distributions

The goal of the analysis presented below is to determine the electron energies at which flux enhancements are most well associated with the EXS_SPW anomalies. To generate distributions of electron fluxes associated with the EXS_SPW anomalies, MPS-LO and MPS-HI fluxes in each channel are averaged over the 30-min interval preceding each EXS_SPW anomaly. These distributions of 30-min averaged fluxes are henceforth referred to as *anomaly distributions*.

Use of a 30-min averaging interval is chosen to capture the substorm injection timescale, e.g., approximate duration of peaks appearing in the MPS-HI fluxes in Fig. 1. The clusters of EXS_SPW anomalies occur during periods of enhanced substorm injections and often anomalies occur in conjunction with individual injections, coincident with peak electron fluxes.

The anomaly distributions are compared with *full distributions* of fluxes averaged over regular 30-min intervals since MPS-HI and MPS-LO began collecting data. The numbers of valid 30-min samples in the GOES-16 and -17 full distributions are approximately 70 000 and 87 000, respectively, again, with differences in totals among MPS channels due to differences in data coverage over the study period.

An example of full and anomaly flux distributions from the GOES-16 MPS-HI ETel-4 E2 channel (centrally viewing telescope, 131 keV) is shown in Fig. 2. The anomaly distribution median is shown by the red dashed vertical line. The full distribution 25th percentile, median, and 75th percentile are shown by the blue dashed vertical lines. In this case, the anomaly distribution median is above the full distribution 75th percentile indicating an association between the EXS_SPW anomalies and elevated flux levels in the GOES-16 MPS-HI ETel-4 E2 channel.

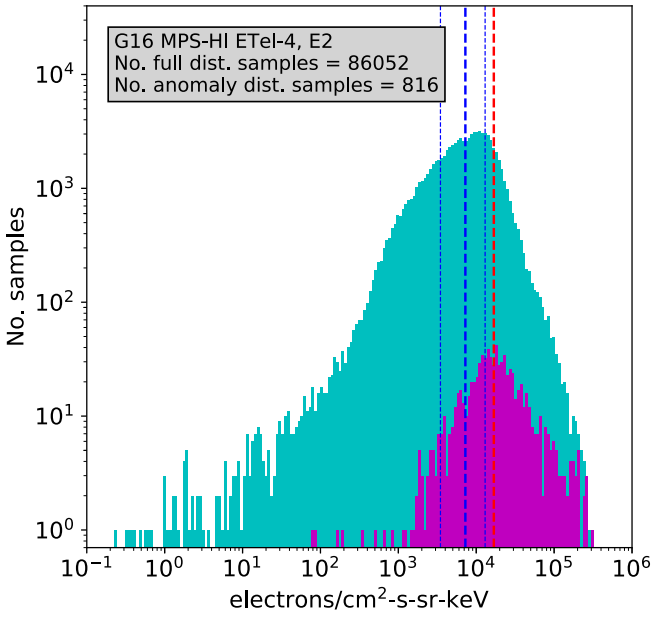

Fig. 2. Examples of full (cyan) and anomaly (magenta) distributions of 30-min averaged fluxes from the GOES-16 MPS-HI ETel-4 E2 (∼130 keV) channel. The anomaly distribution median is shown by the red dashed vertical line. The full distribution 25th percentile, median, and 75th percentile are shown by blue dashed vertical lines. The full distribution percentile at the anomaly distribution median is 85.2.

Three approaches are used to characterize the difference between anomaly and full distributions for all MPS-LO and MPS-HI zone/telescope energy-channel pairs:

1) two-sample Kolmogorov–Smirnov (K–S) test;
2) chi-square test;
3) Full distribution percentile at anomaly distribution median.

The K–S and chi-square tests [31], [32] are well-established statistical tests of the dependence/independence of two distributions. They provide an answer to the question, what is the probability that two random sampling distributions were drawn from the same population? The K–S and Chi-square tests will return a higher test statistic value for greater differences in shape, spread or median between the full and anomaly distributions. The third approach involves use of an inverse percentile function to find the full distribution percentile at the anomaly distribution median flux. An important distinction between the first two statistical tests and the third approach is that, the K–S and chi-square tests are sensitive to any difference in shape between the full and anomaly distributions (e.g., mean, variance, skewness, or kurtosis), whereas the third approach only gives the location of the anomaly distribution median within the full distribution. Another difference is that as the anomaly distribution is shifted to the left of the full distribution, the full distribution percentile at anomaly distribution median continues to decrease, whereas the K–S and chi-square test statistics increase with any deviation of the anomaly distribution from the full distribution. We do not provide a formal justification for the third approach, but it is intuitively appealing and yields approximately the same results as the chi-squared and K–S tests presented below. In each case, the test statistic is taken as a measure of the difference between full and anomaly distributions rather than used to accept or reject a null hypothesis based on a threshold probability value, which is a standard use for the K–S and chi-square tests.

The GOES-16 EXS_SPW anomaly K–S test results are shown in Fig. 3. The MPS-LO and MPS-HI energy channels are listed in order of increasing energy from 30 eV to >2 MeV along the horizontal axis. The vertical axes indicate look directions in south-to-north order, in a fan of look directions symmetric about the geographic equator viewing away from Earth. The vertical axes include 14 MPS-LO zones in the left panel and five MPS-HI telescopes in the right panel.

The GOES-16 telescope energy-channel pair with the maximum K–S statistic value is MPS-HI ETel-1 (viewing 35° above the geographic equator), energy channel E2 (∼130 keV). In general, the K–S statistic values are elevated in the MPS-HI E2 (∼130 keV) and E3 (∼180 keV) energy channels. GOES-16 ETels-4 and -1 look directions usually straddle a perpendicular to the geomagnetic field vector, and ETel-1 usually views pitch angles closest to 90°.

The GOES-17 test results are shown in Fig. 4, here showing the full distribution percentile at the anomaly distribution median in each channel. The GOES-17 maximum statistic value is also in the MPS-HI E2 energy channel. The maximum value is in ETel-4 (viewing along the geographic equator). The GOES-17 ETel-4 look direction was usually closest to perpendicular to the geomagnetic field vector over the data collection period, thus it viewed pitch angles nearest to 90°.

When the GOES-R series spacecraft are in their nominal upright position, the north-to-south order of the MPS-HI electron telescopes is ETel-5, -2, -4, -1, and -3, as shown in Fig. 3. Since GOES-17 has undergone a series of yaw flips since launch, reversing the north-to-south order of MPS-HI telescope numbers with each yaw flip; the GOES-17 data are organized with respect to look direction prior to performing the analysis, and the vertical axes in Fig. 4 are labeled in terms of look directions with respect to the geographic equator. A yaw flip maneuver has not been performed on GOES-16.

TABLE II
TELESCOPE/LOOK-DIRECTION, ENERGY CHANNEL, AND ANOMALY VERSUS FULL DISTRIBUTION TEST STATISTIC AT TEST STATISTIC MAXIMA

	GOES-16	GOES-17
K-S test statistic	ETel-1 (+35°), E2 : 0.396	-35°, E2 : 0.414
Chi-square test statistic	ETel-1 (+35°), E2 : 1850.	0°, E2 : 1560.
Full dist. percentile at anomaly dist. median	ETel-4 (0°), E2 : 85.2	0°, E2 : 86.8

Surface plots analogous to Figs. 3 and 4 showing GOES-16 and -17 results from the other statistical approaches are not included in this article. GOES-16 and -17 maxima from all 3 statistical tests are given in Table II. In all cases, the test statistic values are most elevated in the MPS-HI E2 energy channel and in look directions near 90° pitch angles.

Use of a 30-min averaging interval prior to the anomalies is somewhat arbitrary, but adjusting this interval from 5 min to several hours does not significantly affect the results. Intervals of 5 min, 30 min, and 6 h all yield test statistic maxima in the MPS-HI E2 or E3 energy channel. As an interval of 24 h is approached the maximum approaches lower energies (e.g., maximum in MPS-HI E1 at 24 h). This is because the lower energy fluxes remain significantly elevated over long periods surrounding the anomaly clusters and the contribution of individual injections becomes less significant.

B. Superposed Epoch Analysis

A superposed epoch analysis (SEA) of GOES-16 MPS-LO and MPS-HI zone/telescope averaged fluxes was performed using EXS_SPW anomaly times as an SEA key time for each MPS-LO and MPS-HI channel time series. The SEA results were generated by summing 846 5-min cadence flux time series, each spanning an interval from 12 h preceding to 12 h following each anomaly event, then dividing by the total number of events. Each SEA channel time series is then divided by the mean flux from the full flux distributions of all 5-min flux samples (e.g., mean value of the cyan colored distribution in Fig. 2). This last step normalizes the SEA flux time series so that results from each channel can be easily compared on the same scale. The results are shown in Fig. 5 for a selected set of MPS-LO and MPS-HI channels.

The most striking feature in the SEA results is the peaks in MPS-HI E1–E3 channels ∼30-min prior to the anomaly key time. Injection peaks in the tens to hundreds of kiloelectron volts in the morning sector are common in the MPS-LO and MPS-HI data and are seen over a broad range of local times. The organization of these injection peaks into a single peak preceding the anomaly key time provides strong evidence that electron energies within the MPS-HI E1–E3 (70–180 keV) range are the primary source of the EXS_SPW anomalies.

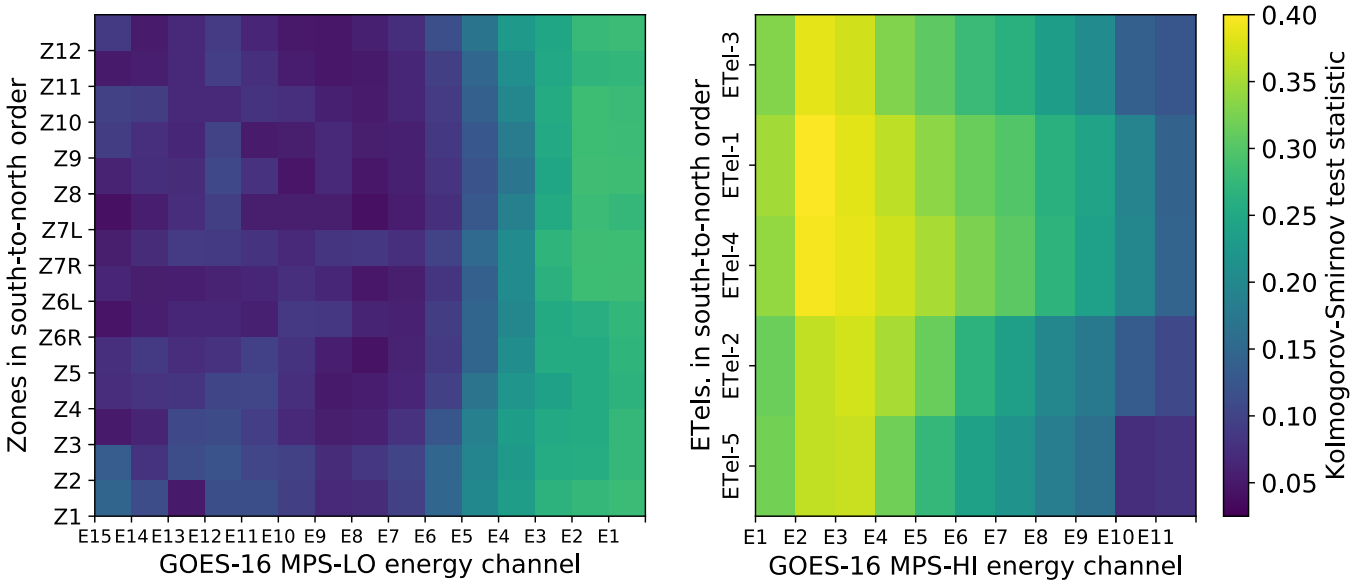

Fig. 3. GOES -16 EXS_SPW anomaly versus full distribution K–S test statistic as a function of energy channel and look-direction. The MPS-LO and MPS-HI energy channels are listed in order of increasing energy from 30 eV to 30 keV (MPS-LO) and from ∼70 keV to >2 MeV (MPS-HI) along the horizontal axes (see Table I for nominal channel energies). The vertical axes indicate look direction in south-to-north order (bottom to top), viewing away from Earth in a fan of look directions symmetric about the geographic equator. The vertical axes include 14 MPS-LO zones in the left and 5 MPS-HI telescopes in the right. MPS-LO/MPS-HI zone/telescope viewing directions are described in Section III-B.

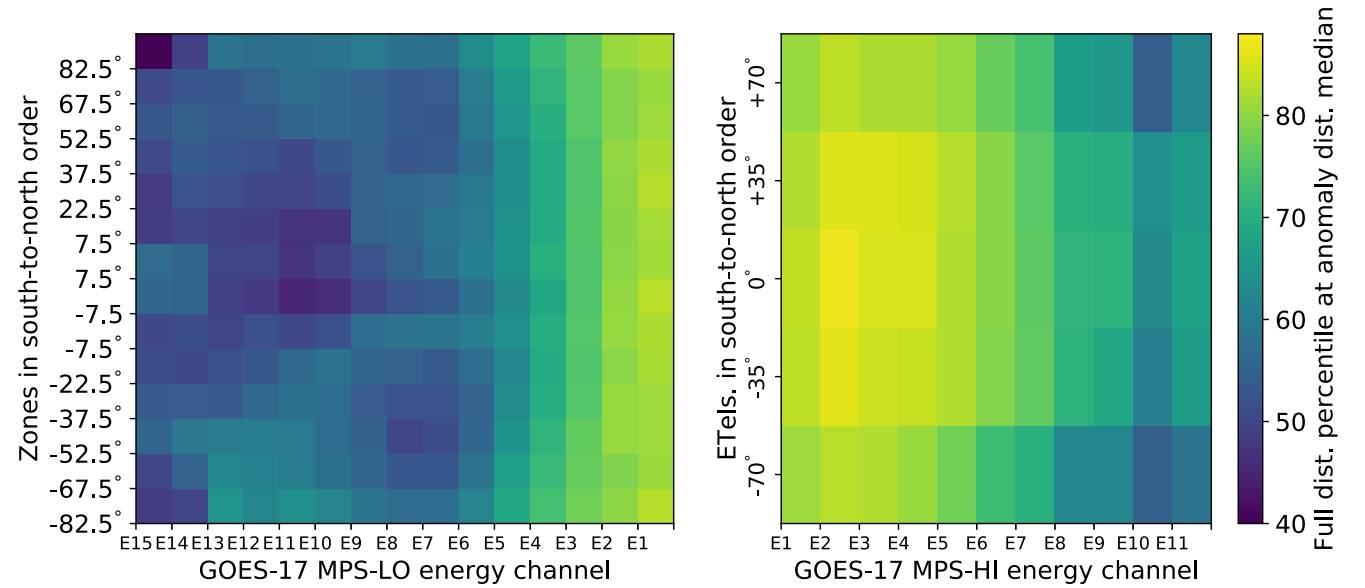

Fig. 4. GOES-17 full distribution percentiles at anomaly distribution medians, presented in the same format as the GOES-16 K–S test statistic results in Fig. 3. The MPS-LO and MPS-HI energy channels are listed in order of increasing energy from 30 eV to 30 keV (MPS-LO) and from ∼70 keV to >2 MeV (MPS-HI) along the horizontal axes (see Table I for nominal channel energies). Since GOES-17 has undergone a series of yaw flips since launch, the vertical axes in the left and right are labeled in terms of telescope/zone look direction with respect to the geographic equator, rather than zone labels and telescope numbers as shown in Fig. 3.

The enhancements in MPS-LO E1 and E2 channels suggest that electrons in the low tens of kiloelectron volts may also contribute to the anomalies, but these SEA analysis enhancements may also be due to a correlation between tens and hundreds of kiloelectron volts electrons during periods of enhanced injections and geomagnetic activity. Similarly, an increase in MPS-HI channels ≥E4 is expected since radiation belt fluxes are in general increasing during periods of geomagnetic activity. The gradual increase in fluxes in MPS-HI ≥E4 channels can also be attributed to a general increase in these channels approaching the dayside and their maxima near noon local time. The GOES orbit intersects the lowest L-shells along its orbit near noon local time due to dayside compression of the Earth's magnetosphere, and in general there is a negative radial gradient in hundreds of kiloelectron volt to megaelectron volt electron fluxes at geosynchronous.

C. Local Time Dependence

A histogram showing the local time dependence of the GOES-16 EXS_SPW anomalies is shown in Fig. 6,

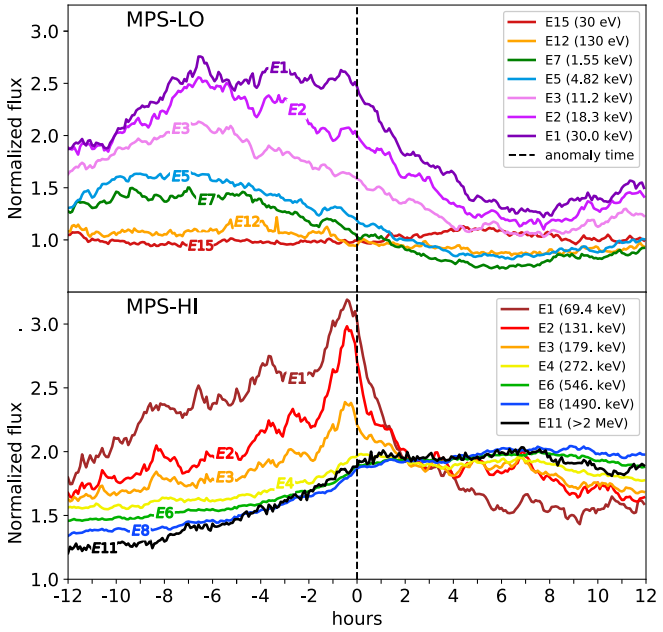

Fig. 5. SEA of GOES-16 MPS-LO and MPS-HI zone/telescope averaged fluxes from selected channels, with the anomaly time used as the SEA key time. The 846 5-min averaged flux time series from each energy channel, spanning the 12 h preceding and following each anomaly (288 samples in each), are summed then divided by the total number of anomalies and normalized by the mean flux.

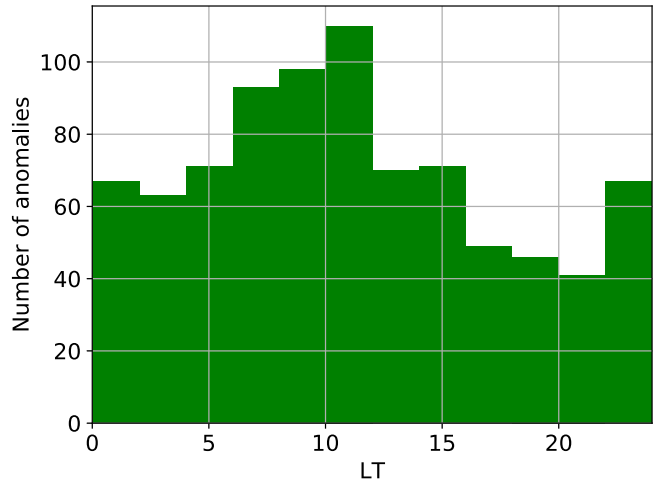

Fig. 6. Local time distribution of anomalies, showing 846 GOES-16 EXS_SPW anomalies sorted into 2-h local time bins. The anomaly occurrence rate is highest in the late morning sector, rising to a peak in the 10–12 local time sector.

where 846 GOES-16 EXS_SPW anomalies are sorted into 2-h local time bins. The anomalies occur at all local times, but the anomaly occurrence rate is higher in the late morning sector, increasing to a peak in the 10–12 local time bin. There is a significant drop to less than half the peak occurrence rate in the postnoon and dusk sectors. Higher anomaly occurrence rates in the morning sector implicate plasma sheet injections as a primary source for the EXS_SPW anomalies. During periods of heightened geomagnetic activity, tens to hundreds of kiloelectron volt electrons are injected earthward from the plasmasheet and propagate sunward in the morning sector. These injections are most prominent in the dawn and late morning sectors, with diminishing intensity thereafter.

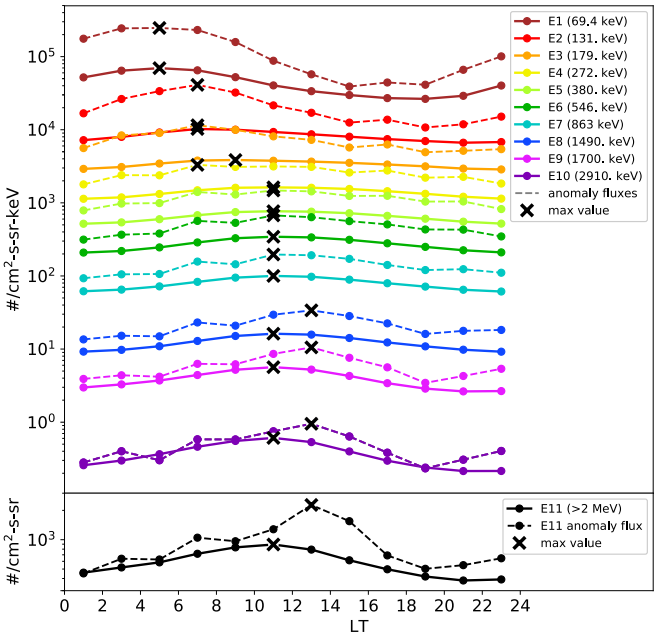

Fig. 7. Average GOES-16 MPS-HI fluxes versus local time, from full (solid) and anomaly (dashed) distributions. The 5-min averaged fluxes are sorted into 2-h local time bins, then local time sector averages are computed in each bin. The anomaly fluxes include all 5-min samples within the 30-min interval preceding each anomaly. An x-symbol indicates the maximum value along each trace.

Fig. 7 shows the local time sector averages of MPS-HI fluxes in ten differential channels (upper panel) and the E11 (>2 MeV) integral channel (lower panel), using 5-min averaged samples from the entire G16 MPS-HI dataset (solid traces) and 5-min averaged samples that fall within 30-min intervals prior to the EXS_SPW anomalies (dashed traces). The samples are binned in local time, then averages are computed within each bin. The fluxes are also telescope-averaged over the five MPS-HI electron telescopes. The maximum value along each trace is indicated by an x-symbol. In general, the lower MPS-HI energy channel fluxes reach a maximum at earlier local times than the higher energy channel fluxes, with the full and anomaly flux maxima spanning local times 5–13.

The asymmetry in anomaly occurrences about noon local time, seen in the histogram in Fig. 6, is reflected in the local time sector averaged MPS-HI channel fluxes below E7 (863 keV). MPS-HI E8–E11 anomaly fluxes have maxima in the postnoon sector, where the anomaly rate drops significantly. It is noteworthy that the peak in anomaly occurrence rate near 11 local time is ∼4 h later than the maximum in the local time averaged MPS-HI E2 flux, which is shown to be most well associated with the anomaly occurrences in the previous section. The above noted delay is in contrast to the ∼30 min delay between the superposition of MPS-HI E1-E3 injection peaks and anomaly key time shown in Fig. 5. Although the anomalies often occur in near conjunction with the injection peaks, the anomalies also occur following extended periods of injections and/or elevated fluxes and during quiet periods.

V. Summary and Discussion

Analysis of enhancements in 30 eV–3 MeV electron fluxes in 25 differential energy channels shows that the EXS_SPW

anomalies are most well associated with enhancements in ∼130-keV electron flux levels. In the GOES-16 MPS-HI ETel-4 E2 channel, the median of the anomaly flux distribution is at the 85th percentile of the full flux distribution, which is significantly higher than at ∼1 keV or >2 MeV, where the anomaly distribution medians are at less than the 65th percentile of the full distributions. The results support shallow internal charging, rather than surface charging by <100-keV electrons or deep dielectric charging by >1-MeV electrons, as the primary source of the EXS_SPW anomalies. This result confirms a provisional conclusion from inspection of Fig. 1 that the anomalies are caused by enhanced electron fluxes in the hundreds of kiloelectron volts.

The EXS_SPW anomalies are also associated with enhanced fluxes near 90° pitch angles. Radiation belt pitch angle distributions are a strong function of local time, with distributions in the 100s of keV typically more peaked ∼90° on the dayside [33], [34]. Since the anomalies occur more frequently on the dayside, we expect the anomalies to be associated with enhanced fluxes near 90° pitch angles.

There is a significant delay between the maximum in MPS-HI E2 sector averaged anomaly flux seen in Fig. 7, near 7-h local time, and the maximum anomaly occurrence rate at ∼11-h local time in Fig. 6. Wrenn and Smith [6] present analysis of geosynchronous surface charging currents estimated from the Special Sensor J-3 (SSJ-3) detector on the geostationary European meteorology spacecraft, METEOSAT-2, and occurrence of spurious status changes in a power supply indicator (A108) on ESA's MARECS-A maritime communications spacecraft. They attribute similar local time differences between maxima in Meteosat-2 SSJ-3 charging currents and occurrence rates of MARECS-A A108 switches to the eastward drift of electrons and a finite charging time.

Internal charging timescales are thought to be many hours to days [3], [6], [7]. Wrenn and Smith [6] also investigated phantom commands on geosynchronous satellites thought to be caused by internal charging and noted the correlation of the anomalies with GOES >2 MeV electron fluxes. These anomalies peaked in the 8–11 local time sector. Wrenn and Smith [6] attribute internal charging at geosynchronous to integrated flux of relativistic electrons over a period of a day or more and suggest that the local time dependence is due to variation in threshold conditions for discharge with local time.

While Fig. 7 shows sector averaged anomaly fluxes versus local-time, the SEA analysis results in Fig. 5 show the averaged anomaly flux time series organized with respect to the anomaly key time. In Fig. 5, the strong peaks in MPS-HI E1-E3 channels are superpositions of injection peaks that are distributed throughout the morning sector. The frequent injection peaks in the morning sector contribute significantly to the heightened E1–E3 fluxes near 6-h local time seen in Fig. 7. If the MPS-HI E1–E3 channel electrons are the dominant cause of the EXS_SPW anomalies, then the local time delay between E1 and E3 maxima in Fig. 7 and maximum anomaly occurrence rate in Fig. 6 could be attributed to a charging/discharging timescale of 30 min to several hours, or local time dependence of conditions more favorable for ESDs.

The maximum anomaly occurrence rate near 11-h local time suggests that electrons in the MPS-HI E5-E7 (380–863keV) energy range may also contribute to the anomalies. However, if energies ∼130 keV are primarily responsible for the EXS_SPW anomaly, it is unlikely that the higher energies contribute significantly, since electron enhancements at 130 keV are more than an order of magnitude greater than at MPS-HI E5–E7 energies. It is also possible that multiple charging sites are responsible for the EXS_SPW anomalies, with some charging sites requiring deeper penetration by electrons at higher energies.

It is not clear what role is played by electron energies <50 keV, which are also enhanced prior to the anomaly key time in the SEA analysis shown in Fig. 5. The generally accepted energy range where there is a transition from surface to internal charging is ∼50–100 keV [1, p. 27]. The statistical analysis presented in Section IV points to internal charging as the primary cause of the EXS_SPW anomalies. Previous studies of internal charging anomalies have implicated energies >200 keV [18], >300 keV [17], and megaelectron volt energies [10], [11], [12], [13], [14], [15]. The EXS_SPW anomaly results presented here are generally in agreement with [17, Fig. 8] showing that the greatest deviation of the SCATHA "extreme [sunlit surface] charging environment" spectrum from the typical electron spectrum occurs at ∼100 keV. To our knowledge, this article is the first report on anomalies supporting shallow internal charging by electrons in the 100–200-keV range. In addition, careful analysis will be needed to determine the role of electron energies outside of this range.

REFERENCES

[1] NASA. (Mar. 3, 2011). *Mitigating in-Space Charging Effects—A Guideline*. NASA Technical Handbook NASA-HDBK-4002A. [Online]. Available: https://standards.nasa.gov/standard/NASA/NASA-HDBK-4002

[2] J. E. Mazur, J. F. Fennell, J. L. Roeder, P. T. O'Brien, T. B. Guild, and J. J. Likar, "The timescale of surface-charging events," *IEEE Trans. Plasma Sci.*, vol. 40, no. 2, pp. 237–245, Feb. 2012, doi: 10.1109/TPS.2011.2174656.

[3] M. F. Thomsen, M. G. Henderson, and V. K. Jordanova, "Statistical properties of the surface-charging environment at geosynchronous orbit," *Space Weather*, vol. 11, no. 5, pp. 237–244, May 2013, doi: 10.1002/swe.20049.

[4] A. Meulenberg Jr., "Evidence for a new discharge mechanism for dielectrics in a plasma," in *Proc. Spacecraft Charging Magnetospheric Plasmas, Symp.*, vol. 47, A. Rosen, Ed. 1976, pp. 237–246.

[5] J. F. Fennell, H. C. Koons, M. W. Chen, and J. B. Blake, "Internal charging: A preliminary environmental specification for satellites," *IEEE Trans. Plasma Sci.*, vol. 28, no. 6, pp. 2029–2036, Dec. 2000, doi: 10.1109/27.902230.

[6] G. L. Wrenn and R. J. K. Smith, "Probability factors governing ESD effects in geosynchronous orbit," *IEEE Trans. Nucl. Sci.*, vol. 43, no. 6, pp. 2783–2789, Dec. 1996, doi: 10.1109/23.556867.

[7] D. J. Rodgers and K. A. Ryden, "Internal charging in space," in *Proc. 7th Spacecraft Charging Technol. Conf.*, R. A. Harris, Ed., Noordwijk, The Netherlands, 2001, p. 25.

[8] A. L. Vampola, "Thick dielectric charging on high-altitude spacecraft," *J. Electrostatics*, vol. 20, no. 1, pp. 21–30, Oct. 1987, doi: 10.1016/0304-3886(87)90083-0.

[9] H. C. Koons et al., "The impact of space environment on space systems," Aerosp. Corp., El Segundo, CA. USA, Tech. Rep., TR-99(1670)-1, 1999.

[10] G. L. Wrenn, "Conclusive evidence for internal dielectric charging anomalies on geosynchronous communications spacecraft," *J. Spacecraft Rockets*, vol. 32, no. 3, pp. 514–520, May 1995.

[11] G. L. Wrenn and A. J. Sims, "Internal charging in the outer zone and operational anomalies," *Radiat. Belts: Models Standards*, vol. 97, pp. 275–278, Jan. 1996.

[12] D. N. Baker, "The occurrence of operational anomalies in spacecraft and their relationship to space weather," *IEEE Trans. Plasma Sci.*, vol. 28, no. 6, pp. 2007–2016, Dec. 2000, doi: 10.1109/27.902228.

[13] N. Iucci et al., "Spacecraft operational anomalies and space weather impact hazards," *Adv. Space Res.*, vol. 37, no. 1, pp. 184–190, Jan. 2006, doi: 10.1016/j.asr.2005.03.028.

[14] H. Choi et al., "Analysis of GEO spacecraft anomalies: Space weather relationships," *Space Weather*, vol. 9, no. 6, Jun. 2011, Art. no. S06001, doi: 10.1029/2010sw000597.

[15] K. A. Ryden, A. D. P. Hands, C. I. Underwood, and D. J. Rodgers, "Internal charging measurements in medium Earth orbit using the SURF sensor: 2005–2014," *IEEE Trans. Plasma Sci.*, vol. 43, no. 9, pp. 3014–3020, Sep. 2015.

[16] D. N. Baker, S. Kanekal, J. B. Blake, B. Klecker, and G. Rostoker, "Satellite anomalies linked to electron increase in the magnetosphere," *Eos, Trans. Amer. Geophys. Union*, vol. 75, no. 35, pp. 401–405, Aug. 1994.

[17] J. F. Fennell, H. C. Koons, J. L. Roeder, and J. B. Blake, "Spacecraft charging: Observations and relationship to satellite anomalies," Space Missile Syst. Center Air Force Materiel Command, El Segundo, CA, USA, Tech. Rep. SMC-TR-01-18, TR-2001 (8570)-5, Aug. 2001. [Online]. Available: https://apps.dtic.mil/sti/tr/pdf/ADA394826.pdf

[18] D. Ferguson, W. Denig, and J. Rodriguez, "Plasma conditions during the Galaxy 15 anomaly and the possibility of ESD from subsurface charging," in *Proc. 49th AIAA Aerospace Sciences Meeting Including New Horizons Forum Aerospace Expo.*, Sep. 2011, p. 1061.

[19] W. H. Farthing, J. P. Brown, and W. C. Bryant, "Differential spacecraft charging on the geostationary operational satellites," NASA, Washington, DC, USA, Memo, Tech. Rep., TM-83908, 1982.

[20] J. F. Fennell, J. L. Roeder, G. A. Berg, and R. K. Elsen, "HEO satellite frame and differential charging and SCATHA low-level frame charging," *IEEE Trans. Plasma Sci.*, vol. 36, no. 5, pp. 2271–2279, Oct. 2008, doi: 10.1109/TPS.2008.2003441.

[21] W. Q. Lohmeyer and K. Cahoy, "Space weather radiation effects on geostationary satellite solid-state power amplifiers," *Space Weather*, vol. 11, no. 8, pp. 476–488, Aug. 2013, doi: 10.1002/swe.20071.

[22] B. K. Dichter et al., "Specification, design, and calibration of the space weather suite of instruments on the NOAA GOES-R program spacecraft," *IEEE Trans. Nucl. Sci.*, vol. 62, no. 6, pp. 2776–2783, Dec. 2015, doi: 10.1109/TNS.2015.2477997.

[23] B. T. Kress, J. V. Rodriguez, and T. G. Onsager, "The GOES-R space environment in situ suite (SEISS): Measurement of energetic particles in geospace," in *The Goes-R Series*, J. S. Goodman, T. J. Schmit, J. Daniels, and R. J. Redmon, Eds. Amsterdam, The Netherlands: Elsevier, pp. 243–250, 2020, doi: 10.1016/B978-0-12-814327-8.00020-2.

[24] P. C. Chamberlin, T. N. Woods, F. G. Eparvier, and A. R. Jones, "Next generation X-ray sensor (XRS) for the NOAA GOES-R satellite series," *Proc. SPIE*, vol. 7438, May 2009, Art. no. 743802, doi: 10.1117/12.826807.

[25] F. G. Eparvier, D. Crotser, A. R. Jones, W. E. McClintock, M. Snow, and T. N. Woods, "The extreme ultraviolet sensor (EUVS) for GOES-R," *Proc. SPIE*, vol. 7438, Sep. 2009, Art. no. 743804, doi: 10.1117/12.826445.

[26] A. Boudouridis, J. V. Rodriguez, B. T. Kress, B. K. Dichter, and T. G. Onsager, "Development of a bowtie inversion technique for real-time processing of the GOES-16/-17 SEISS MPS-HI electron channels," *Space Weather*, vol. 18, no. 4, Apr. 2020, Art. no. e2019SW002403, doi: 10.1029/2019sw002403.

[27] C. E. Mallon, M. J. Treadaway, T. M. Flanagan, E. P. Wenaas, and R. Denson, "High-energy electron-induced discharges and SGEMP modification in cables," AFWL ECEMP Phenomenol. Memo, USAF Weapons Lab, Albuquerque, NM, USA, Tech. Rep., 29, 1979.

[28] K. Kadinsky-Cade et al., "Defense Meteorological Satellite program-special sensor J5 (SSJ5) sensor number 16 (SN16) calibration report," Air Force Res. Lab, Kirtland AFB, NM, USA, Tech. Rep., AFRL-RV-PS-TP-2016-0007, 2002. [Online]. Available: https://apps.dtic.mil/sti/citations/AD1027803

[29] R. J. Redmon, W. F. Denig, L. M. Kilcommons, and D. J. Knipp, "New DMSP database of precipitating auroral electrons and ions," *J. Geophys. Res.: Space Phys.*, vol. 122, no. 8, pp. 9056–9067, Aug. 2017, doi: 10.1002/2016ja023339.

[30] D. N. Baker et al., "Multiyear measurements of radiation belt electrons: Acceleration, transport, and loss," *J. Geophys. Res.: Space Phys.*, vol. 124, no. 4, pp. 2588–2602, Apr. 2019, doi: 10.1029/2018ja026259.

[31] I. M. Chakravarti, R. G. Laha, and J. Roy, *Handbook of Methods of Applied Statistics. Volume I: Techniques of Computation, Descriptive Methods, and Statistical Inference*. Hoboken, NJ, USA: Wiley, 1967, pp. 392–394.

[32] G. W. Snedecor and W. G. Cochran, *Statistical Methods*, 8th ed. Ames, IA, USA: Iowa State Univ. Press, 1989.

[33] X. Gu, Z. Zhao, B. Ni, Y. Shprits, and C. Zhou, "Statistical analysis of pitch angle distribution of radiation belt energetic electrons near the geostationary orbit: CRRES observations," *J. Geophys. Res.: Space Phys.*, vol. 116, no. A1, Jan. 2011. [Online]. Available: https://agupubs.onlinelibrary.wiley.com/doi/full/10.1029/2010JA016052, doi: 10.1029/2010ja016052.

[34] J. L. Gannon, X. Li, and D. Heynderickx, "Pitch angle distribution analysis of radiation belt electrons based on combined release and radiation effects satellite medium electrons a data," *J. Geophys. Res.: Space Phys.*, vol. 112, no. 5, May 2007, Art. no. A05212, doi: 10.1029/2005ja011565.